

Localized dielectric breakdown and antireflection coating in metal-oxide-semiconductor photoelectrodes

Li Ji^{1,2*}†, Hsien-Yi Hsu^{2†}, Xiaohan Li¹, Kai Huang¹, Ye Zhang¹, Jack C. Lee¹, Allen J. Bard² and Edward T. Yu¹

Silicon-based photoelectrodes for solar fuel production have attracted great interest over the past decade, with the major challenge being silicon's vulnerability to corrosion. A metal-insulator-semiconductor architecture, in which an insulator film serves as a protection layer, can prevent corrosion but must also allow low-resistance carrier transport, generally leading to a trade-off between stability and efficiency. In this work, we propose and demonstrate a general method to decouple the two roles of the insulator by employing localized dielectric breakdown. This approach allows the insulator to be thick, which enhances stability, while enabling low-resistance carrier transport as required for efficiency. This method can be applied to various oxides, such as SiO₂ and Al₂O₃. In addition, it is suitable for silicon, III-V compounds, and other optical absorbers for both photocathodes and photoanodes. Finally, the thick metal-oxide layer can serve as a thin-film antireflection coating, which increases light absorption efficiency.

Solar fuel production by semiconductor photoelectrochemical (PEC) water splitting entails the conversion of water by solar radiation into a storable clean fuel. Tremendous effort has been directed towards finding efficient and stable semiconductor materials for this purpose, including silicon^{1–10}, various oxides^{11–15} and III-V compounds¹⁶. Oxides are relatively stable in aqueous environments, but their wide bandgaps limit light absorption. Si and III-V compounds have bandgaps well-suited to absorbing a large portion of the solar spectrum, but suffer from poor stability in aqueous electrolyte. Various protection coating strategies have therefore been proposed to stabilize semiconductor surfaces in aqueous solution. Early attempts to extend photoelectrode lifetime include depositing a thin film of noble metal, such as Ir or Pt, onto silicon¹⁷. However, a direct metal/semiconductor contact often induces Fermi-level pinning, which reduces band bending in the semiconductor and decreases the photovoltage¹⁸. Inserting a thin metal-oxide or metal-nitride layer can reduce or eliminate Fermi-level pinning on elemental semiconductors¹⁸. Thus, a metal-insulator-semiconductor (MIS) architecture has been widely used for silicon-based photoelectrodes.

Figure 1a shows a schematic of a MIS photoelectrode. When illuminated, photogenerated minority carriers in the semiconductor tunnel through the insulating layer to the metal catalyst, where water oxidation or reduction takes place. The insulator layer must protect the semiconductor from corrosion and, simultaneously, allow efficient transport of electrons or holes. High-quality ultrathin metal oxides, such as TiO₂, SiO₂ and NiO_x, have been used as tunnel layers by many groups^{3,5,8}. However, there is still a trade-off between efficiency and stability. Carrier tunnelling probabilities decay exponentially with increasing metal-oxide thickness, so an ultrathin film (<4 nm) is usually required. In this case, however,

stability may be problematic over extended periods of time, as in the pitting corrosion initiated by the appearance of a single pinhole. In the field of anti-corrosion coatings, 50 nm is a common thickness for achieving long-term stability¹⁹. Hence, the two roles of the insulator, as a protection layer and a tunnel layer, must be decoupled. Our previous work utilized epitaxial SrTiO₃ grown on p-Si for hydrogen production¹⁰. Because the conduction band offset between SrTiO₃ and p-Si is small, electron transport in the SrTiO₃ layer is via band conduction instead of tunnelling. The photocurrent decreases only slightly with increasing oxide thickness. However, this is not applicable to n-Si due to the large valence band offset. Recently, Hu *et al.* and Seger *et al.* demonstrated a thick TiO₂ conductive protection layer deposited by either atomic layer deposition (ALD) or sputtering for n-type and p-type silicon photoelectrodes, respectively^{4,20}. Carrier transport in these structures is facilitated by the high concentration of defects in TiO₂. However, this method is likely to be difficult to generalize to other oxides, and may also be impeded, in the case of ALD, by slow deposition rates.

Defect formation and migration to increase oxide conductivity can also be induced electrically, most commonly by applying an external electric field. Indeed, resistive switching random access memory (ReRAM) based on this concept has been widely studied^{21–23}. Inspired by this idea that the intrinsic conductivity of various metal oxides can be changed electrically, in this paper we demonstrate a general method for enhancing the effective conductivity of a thick oxide layer in MIS photoelectrodes by employing localized dielectric breakdown, as shown in Fig. 1b. In this approach, a voltage applied across the MIS structure induces formation of a localized electrically conducting filament through the oxide. This filament allows photogenerated carriers in the

¹Microelectronics Research Center, Department of Electrical and Computer Engineering, The University of Texas at Austin, Austin, Texas 78712, USA.

²Center for Electrochemistry, Department of Chemistry and Biochemistry, The University of Texas at Austin, Austin, Texas 78712, USA. †These authors contributed equally to this work. *e-mail: nmgjili@utexas.edu

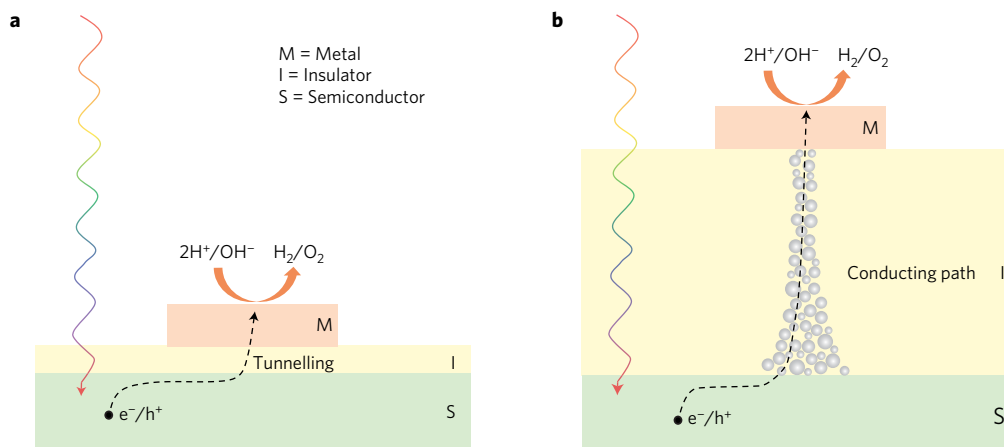


Figure 1 | Metal-insulator-semiconductor photoelectrodes. Schematics of MIS photoelectrode for water reduction/oxidation with an ultrathin tunnelling layer (a) and a thick insulating layer with localized conducting path (b).

semiconductor to flow easily to the metal catalyst layer. In addition, since the metal oxide need not be atomically thin, it can also be used to provide antireflection functionality for improving light absorption—thereby further increasing efficiency²⁰.

Dielectric breakdown and PEC performance

Permalloy ($\text{Ni}_{81}\text{Fe}_{19}$) was used as the oxygen evolution reaction (OER) catalyst for all photoanodes in this work. For the hydrogen evolution reaction (HER) catalyst on photocathodes, 20nmTi/30nmPt bilayer metallization was used. All the OER and HER catalysts were patterned using photolithography and a lift-off process with various feature and pitch sizes. MIS photoelectrodes with several different metal oxides, including Al_2O_3 and TiO_2 , deposited onto Si or GaAs substrates by various methods were also fabricated and tested. Here, we show only representative results with 30 nm thermally grown SiO_2 as the oxide layer. After fabrication of the photoelectrodes, the localized dielectric breakdown procedure is performed. Detailed descriptions and optimization of the breakdown process can be found in Supplementary Figs 2–5. Supplementary Fig. 2(B) shows a typical electrical field versus current curve during breakdown, with the electrical field ramped linearly from 0 MV cm^{-1} to 16 MV cm^{-1} and back to 0 MV cm^{-1} , for n-Si/30nm SiO_2 /150nm $\text{Ni}_{81}\text{Fe}_{19}$. The breakdown field is 9 MV cm^{-1} , a typical value for thermal silicon oxides. The J - V characteristics before and after breakdown are shown in Fig. 2a. The current density is obtained by dividing the current flow on a single metal dot by the square of the periodical pitch size of the array structures. Before breakdown, the current is below the measurement noise level. After breakdown, the current density increases by several orders of magnitude. Since the substrate is n-Si, a negative bias applied to the top metal contact induces upward band bending and accumulation of holes in silicon, corresponding to the working condition of photoanodes. Electrical conductivity at negative bias is therefore critical to PEC photoanode performance. Figure 2a and Supplementary Fig. 5(C) show that the current density on a single 60- μm -diameter dot, normalized to an area of 120 $\mu\text{m} \times 120 \mu\text{m}$, which corresponds to the periodicity of the dot array, can reach ~ 20 –28 mA cm^{-2} (at the 75th percentile) or higher, already sufficient for a high-performance photoanode. Figure 2b shows the temperature dependence of I - V curves in dry condition, revealing ohmic-like conduction within the temperature range studied. Figure 2c is the dry I - V measurement under illumination, confirming the photovoltaic effect.

PEC performance for Si- and GaAs-based photoanodes is shown in Fig. 2d. The photocurrent for samples not subjected to breakdown is zero over the range of potentials applied. After the breakdown

process, clear photoresponse with chopped light is observed. The highest photocurrent density and photovoltage are 9 mA cm^{-2} and 280 mV, respectively. Compared with previous works^{1–7}, the relatively low photocurrent density and photovoltage may result from loss through the breakdown path. The photovoltage was estimated by comparing the onset for OER to the thermodynamic potential. The sample area is 3 mm^2 , containing 1,000 metal dots (60 μm in diameter) arranged in a square array with a period of 120 μm , all of which were subjected individually to the breakdown process. Approaches for automating the breakdown process would be very feasible using mainstream chip testing tools and procedures. To demonstrate the applicability of this method to other semiconductors, an n-GaAs/1.5nm Al_2O_3 /30nm SiO_2 /150nm $\text{Ni}_{81}\text{Fe}_{19}$ device was also fabricated. The thin layer of Al_2O_3 grown by thermal ALD passivates the GaAs surface—a widely used approach for GaAs-based MOSFETs. The SiO_2 layer was grown by plasma-enhanced atomic layer deposition (PEALD) in remote mode to ensure high quality. The PEC performance after breakdown is shown by the blue line in Fig. 2d. The result is similar to that of the silicon-based photoanode. This method can also be used for photocathodes, as shown in Fig. 2e. For a p-Si/30nm SiO_2 /20nmTi/30nmPt photocathode structure, without breakdown, the photocurrent is zero. After breakdown, the photocurrent density increases to 9 mA cm^{-2} . However, the photovoltage is only 200 mV, smaller than that of the photoanodes. Figure 2f shows a chronoamperometric test of the silicon photocathode, confirming stability after 40 h in H_2SO_4 .

Integration of antireflection functionality

The increased oxide layer thickness and flexibility to incorporate different, multiple oxide materials using this approach also enable antireflection functionality to be achieved. Figure 3a,b shows simulation results of optical reflectance versus wavelength with normally incident light for a variety of oxide layer structures in an aqueous environment. As we see in Fig. 3a,b, the reflectance is greatly reduced and the oxide layer structures can be optimized by integrating the optical transmittance weighted by the solar spectrum over wavelength, as described in Supplementary Section IV. As illustration examples, the optimized thicknesses shown in Fig. 3b for $\text{SiO}_2/\text{TiO}_2$ and $\text{Al}_2\text{O}_3/\text{TiO}_2$ oxide stacks were obtained by this method. It is worth noting that TiO_2 is chosen as top layer for photoanodes due to its better anti-corrosion properties in an alkaline environment, compared with SiO_2 and Al_2O_3 . For bare silicon, the reflectance remains above 30% over the entire wavelength range shown. For the optimized $\text{SiO}_2/\text{TiO}_2$ and $\text{Al}_2\text{O}_3/\text{TiO}_2$ structures, the simulated optical reflectance is dramatically reduced. Photographs of real samples with optimized

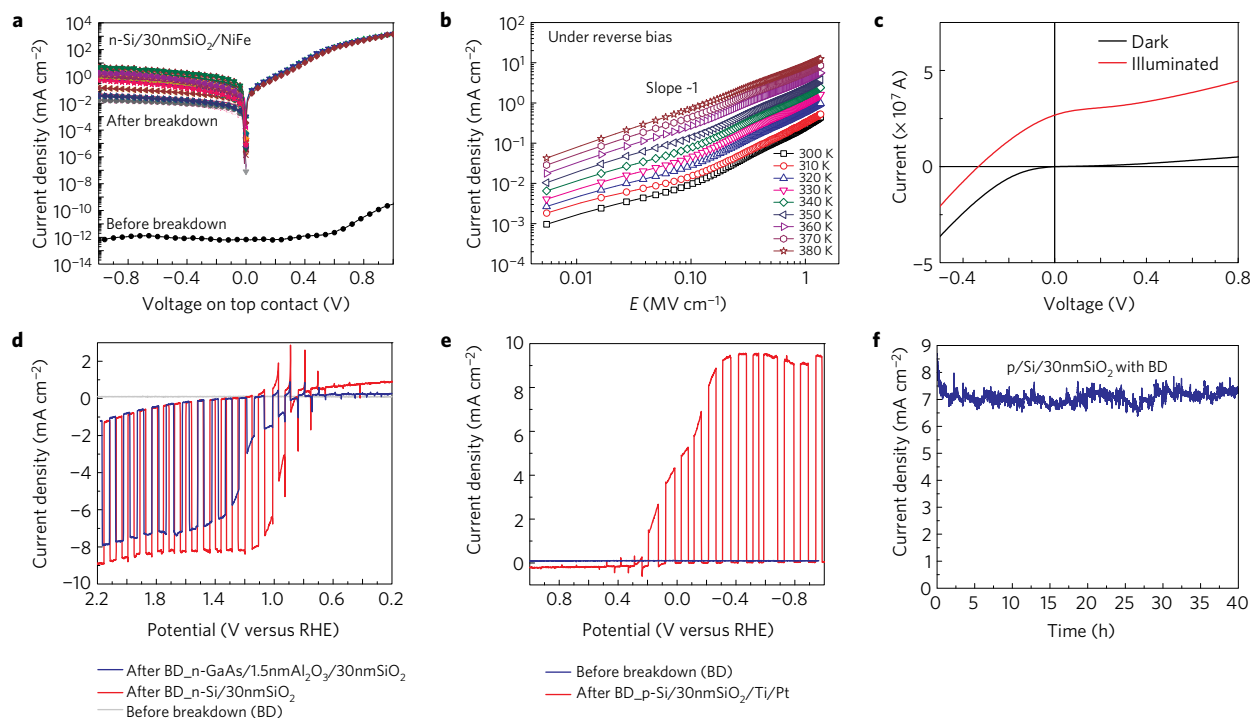


Figure 2 | Electrical and photoelectrochemical characterization. **a**, Dry J - V characteristics of n -Si/30nmSiO₂/150nmNi₈₁Fe₁₉ MIS devices before and after breakdown for a 60- μ m-diameter metal dot contact. **b**, J - E characteristics of the breakdown for temperature from 300 K to 380 K, demonstrating an approximately linear relationship between current and voltage. Metal catalyst contacts were patterned in a square array, 60- μ m-diameter dots with a period of 120 μ m. Every dot was subjected to the electrical breakdown process. **c**, Dry I - V measurements under 100 mW cm⁻² white light illumination for one 60- μ m-diameter metal dot on a p -Si/30nmSiO₂/20nmTi/30nmPt sample. **d**, Linear sweep voltammetry (LSV) curves in 1M KOH solutions for n -Si/30nmSiO₂/150nmNi₈₁Fe₁₉ and n -GaAs/1.5nmAl₂O₃/30nmSiO₂/150nmNi₈₁Fe₁₉ with/without breakdown. **e**, LSV of p -Si/30nmSiO₂/20nmTi/30nmPt with and without breakdown in 0.5M H₂SO₄. The light is chopped when performing LSV and the illumination source light intensity is calibrated to 100 mW cm⁻². **f**, Chronoamperometry of p -Si/30nmSiO₂/150nmNi₈₁Fe₁₉ with breakdown in 1M H₂SO₄ solution. The total area exposed to solutions in **d-f** is 3 mm² for each measurement.

thickness for different thin-film materials are shown as insets in Fig. 3a. The incident-photon-to-current conversion efficiency (IPCE) measured for samples with different oxide thickness and material combinations are shown in Fig. 3c. Samples with lower reflectance as simulated in Fig. 3b exhibit higher IPCE values over the entire visible light wavelength range, confirming the efficacy of this approach.

Permalloy as a novel OER catalyst

Catalysts also play a key role in determining photoelectrode efficiency. The overpotential for overall water splitting is constrained primarily by the sluggish kinetics of the OER on the anode²⁴. IrO₂ and RuO₂ are common commercial OER catalysts, but suffer from high cost. Ni was found long ago to exhibit electrocatalytic activity for OER, and introduction of Fe impurities in Ni can greatly lower the OER overpotential²⁵. Recently, NiFe layered double hydroxide (NiFe-LDH) has received great attention as a highly efficient OER catalyst^{24,26,27}, but this material is difficult to incorporate into MIS photoelectrodes. First, the electrical conductivity of NiFe-LDH is low, as is typical for hydroxides²⁴. In this work, metal catalysts serve as a top contact when performing dielectric breakdown, and good electrical conductivity is required. Second, recent work has shown that using island-like metal catalyst structures can be highly beneficial^{5,10}. NiFe-LDH is typically prepared by electrodeposition, and patterning of array structures is challenging. Here, we employ Permalloy (Ni₈₁Fe₁₉), a widely used material in the electronics and storage industries, as an efficient earth-abundant OER catalyst. Permalloy can be deposited by e-beam evaporation or sputtering, and patterned by standard photolithography. Recent work has

shown that the optimum ratio of Ni to Fe for catalytic performance is Ni:Fe=4:1, essentially identical to the composition of Permalloy²⁸.

To study catalytic activity, Ni₈₁Fe₁₉ and Ni thin films were deposited on Au substrates with e-beam evaporation. The OER characteristics in 1M KOH with a standard three-electrode system are shown in Fig. 4a. Ni₈₁Fe₁₉ electrodes show a sharp onset at 1.5 V and require only 300 mV overpotential versus E(H₂O/O₂) to reach a current density of 10 mA cm⁻², which is better than IrO₂ and among the best active metal OER catalysts, as shown in Supplementary Table 1. Pure Ni electrodes exhibit inferior OER activity, confirming the benefit of Ni doping with Fe²⁸. As shown in Fig. 4b, the Tafel slope for Ni₈₁Fe₁₉ is 36 mV dec⁻¹, indicating fast electron and mass transfer between catalyst and electrolyte, compared to 60 mV dec⁻¹ for Ni. X-ray photoelectron spectra (XPS) for Ni₈₁Fe₁₉ electrodes under different conditions are shown in Supplementary Fig. 7(D),(E). For as-deposited samples, the XPS data show that the metallic and oxide phases for both Ni and Fe are present, resulting from the formation of native oxides²⁹. After an OER test, the Ni 2p_{3/2} peaks are shifted to higher binding energy, indicating a transformation from NiO to Ni(OH)₂ (ref. 30). After 60s Ar⁺ sputtering (etch rate ~0.5 nm s⁻¹), metallic peaks for Ni (852.0, 869.3 eV) and Fe (706.5, 719.9 eV) are recovered. A large reduction of the O 1s peak is also observed (Supplementary Fig. 7). These results indicate that only the surface of Ni₈₁Fe₁₉ is oxidized during OER. The bulk of the thin film is preserved as highly conductive metal.

In summary, we have proposed a general method for resolving the trade-off between efficiency and stability of metal-oxide-semiconductor photoelectrodes, by employing dielectric

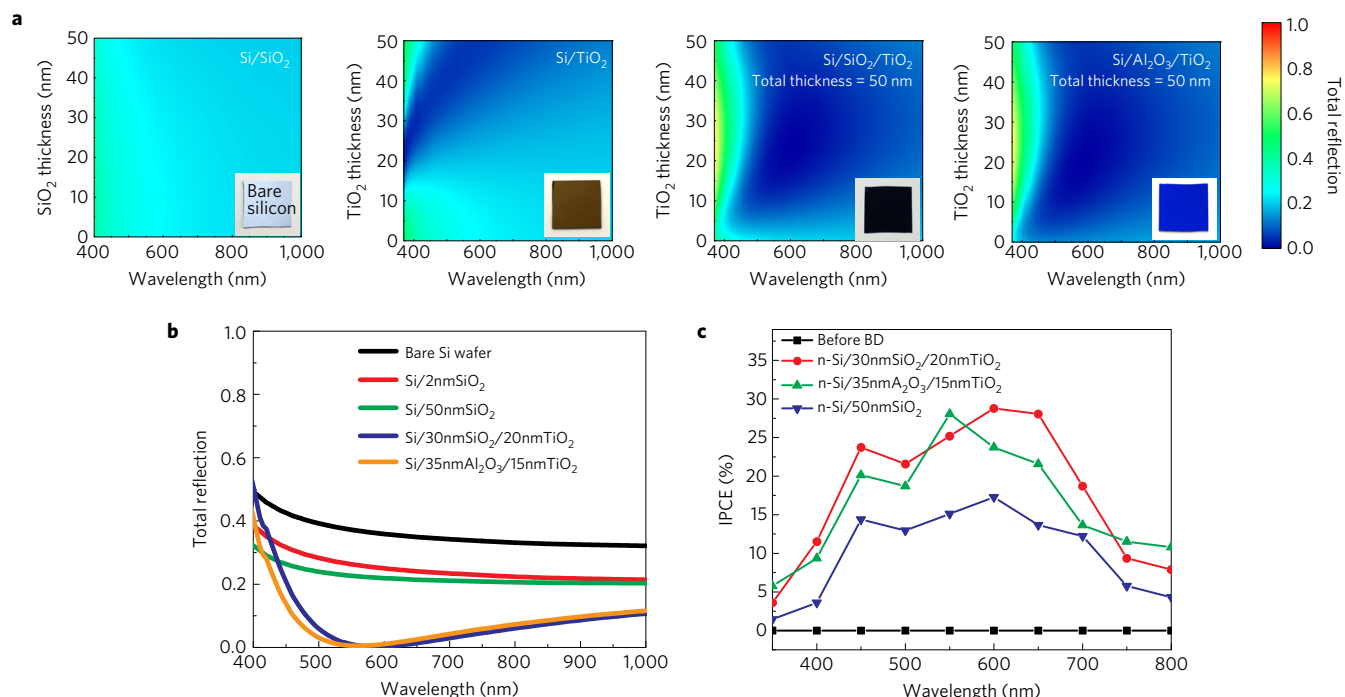


Figure 3 | Antireflection coating and PEC performance. **a**, Numerical simulation of total reflection versus oxide thickness for various oxides on silicon. The global environment is water. The inset is a picture for a bare silicon wafer and samples with oxide thickness optimized as shown in **b**. **b**, Total calculated reflection of various samples with optimized oxide thickness. The optimization calculation can be found in Supplementary Fig. 8. The samples with 30nmSiO₂/20nmTiO₂ and 35nmAl₂O₃/15nmTiO₂ show clear antireflection behaviour arising from the presence of the oxide layers. **c**, IPCE measurements (with 1.6 V bias versus RHE) for samples with different oxide thickness and material combinations. The metal catalyst array is 100- μ m-diameter dots in a square array with a period of 200 μ m for all samples. Higher IPCE for the SiO₂/TiO₂ and Al₂O₃/TiO₂ structures is clearly observed.

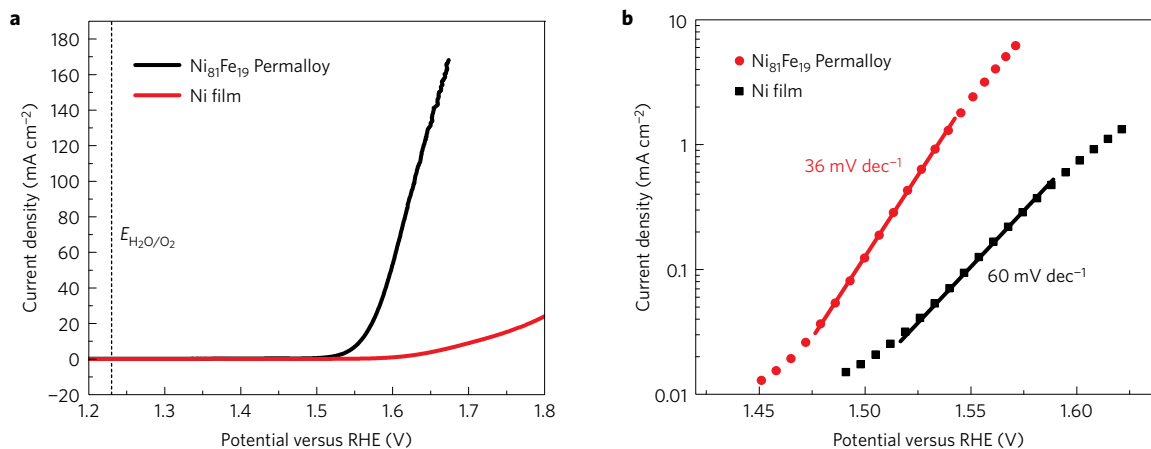


Figure 4 | Ni₈₁Fe₁₉ catalytic performance. **a**, **b**, OER polarization curves (**a**) and Tafel plots (**b**) for e-beam evaporated Ni₈₁Fe₁₉ and Ni thin films in 1M KOH solutions with 95% iR-compensation. The scan rates are 5 mV s⁻¹ and 0.1 mV s⁻¹, respectively.

breakdown. This approach allows the oxide layer to be thick, which enhances stability, while enabling facile carrier transport as required for efficiency. We have demonstrated this method is applicable to various oxides and various semiconductors for either the photocathode or the photoanode. In addition, antireflection functionality can be incorporated due to the increased oxide thickness and multiple oxide layer combinations. Therefore, this approach is fairly general, and is expected to accelerate the pace of development of practical solar-fuel photocatalysts systems.

Methods

Methods and any associated references are available in the [online version of the paper](#).

Received 30 September 2015; accepted 1 August 2016; published online 7 November 2016

References

- Boettcher, S. W. *et al.* Energy-conversion properties of vapor-liquid-solid-grown silicon wire-array photocathodes. *Science* **327**, 185–187 (2010).
- Reece, S. Y. *et al.* Wireless solar water splitting using silicon-based semiconductors and earth-abundant catalysts. *Science* **334**, 645–648 (2011).
- Kenney, M. J. *et al.* High-performance silicon photoanodes passivated with ultrathin nickel films for water oxidation. *Science* **342**, 836–840 (2013).
- Hu, S. *et al.* Amorphous TiO₂ coatings stabilize Si, GaAs, and GaP photoanodes for efficient water oxidation. *Science* **344**, 1005–1009 (2014).

- Esposito, D. V., Levin, I., Moffat, T. P. & Talin, A. A. H₂ evolution at Si-based metal–insulator–semiconductor photoelectrodes enhanced by inversion channel charge collection and H spillover. *Nat. Mater.* **12**, 562–568 (2013).
- Chen, Y. W. *et al.* Atomic layer-deposited tunnel oxide stabilizes silicon photoanodes for water oxidation. *Nat. Mater.* **10**, 539–544 (2011).
- Hou, Y. D. *et al.* Bioinspired molecular co-catalysts bonded to a silicon photocathode for solar hydrogen evolution. *Nat. Mater.* **10**, 434–438 (2011).
- Dasgupta, N. P., Liu, C., Andrews, S., Prinz, F. B. & Yang, P. Atomic layer deposition of platinum catalysts on nanowire surfaces for photoelectrochemical water reduction. *J. Am. Chem. Soc.* **135**, 12932–12935 (2013).
- Hill, J. C., Landers, A. T. & Switzer, J. A. An electrodeposited inhomogeneous metal–insulator–semiconductor junction for efficient photoelectrochemical water oxidation. *Nat. Mater.* **14**, 1150–1155 (2015).
- Ji, L. *et al.* A silicon-based photocathode for water reduction with an epitaxial SrTiO₃ protection layer and a nanostructured catalyst. *Nat. Nanotech.* **10**, 84–90 (2015).
- Warren, S. C. *et al.* Identifying champion nanostructures for solar water-splitting. *Nat. Mater.* **12**, 842–849 (2013).
- Liao, L. *et al.* Efficient solar water-splitting using a nanocrystalline CoO photocatalyst. *Nat. Nanotech.* **9**, 69–73 (2013).
- Chen, X. B., Liu, L., Yu, P. Y. & Mao, S. S. Increasing solar absorption for photocatalysis with black hydrogenated titanium dioxide nanocrystals. *Science* **331**, 746–750 (2011).
- Shi, J. *et al.* Interface engineering by piezoelectric potential in ZnO-based photoelectrochemical anode. *Nano Lett.* **11**, 5587–5593 (2011).
- Tilley, S. D., Cornuz, M., Sivula, K. & Gratzel, M. Light-induced water splitting with hematite: improved nanostructure and iridium oxide catalysis. *Angew. Chem. Int. Ed.* **49**, 6405–6408 (2010).
- Khaselev, O. & Turner, J. A. A monolithic photovoltaic-photoelectrochemical device for hydrogen production via water splitting. *Science* **280**, 425–427 (1998).
- Fan, F. R. F., Keil, R. G. & Bard, A. J. Semiconductor electrodes. 48. Photooxidation of halides and water on n-silicon protected with silicide layers. *J. Am. Chem. Soc.* **105**, 220–224 (1983).
- Kobayashi, M., Kinoshita, A., Saraswat, K., Wong, H. S. P. & Nishi, Y. Fermi-level depinning in metal/Ge Schottky junction and its application to metal source/drainage NMOSFET. *2008 Symposium on VLSI Technology, Digest of Technical Papers* 54–55 (2008).
- Shan, C., Hou, X. & Choy, L. K. Corrosion resistance of TiO₂ films grow by atomic layer deposition. *Surf. Coat. Technol.* **202**, 2399–2402 (2008).
- Seger, B. *et al.* Using TiO₂ as a conductive protective layer for photocathodic H₂ evolution. *J. Am. Chem. Soc.* **135**, 1057–1064 (2013).
- Strukov, D. B., Snider, G. S., Stewart, D. R. & Williams, R. S. The missing memristor found. *Nature* **453**, 80–83 (2008).
- Ji, L. *et al.* Integrated one diode–one resistor architecture in nanopillar SiO_x resistive switching memory by nanosphere lithography. *Nano Lett.* **14**, 813–818 (2014).
- Yu, S. M., Chen, H. Y., Gao, B., Kang, J. F. & Wong, H. S. P. HfO_x-based vertical resistive switching random access memory suitable for bit-cost-effective three-dimensional cross-point architecture. *ACS Nano* **7**, 2320–2325 (2013).
- Gong, M. *et al.* An advanced Ni–Fe layered double hydroxide electrocatalyst for water oxidation. *J. Am. Chem. Soc.* **135**, 8452–8455 (2013).
- Corrigan, D. A. The catalysis of the oxygen evolution reaction by iron impurities in thin film nickel oxide electrodes. *J. Electrochem. Soc.* **134**, 377–384 (1987).
- Louie, M. W. & Bell, A. T. An investigation of thin-film Ni–Fe oxide catalysts for the electrochemical evolution of oxygen. *J. Am. Chem. Soc.* **135**, 12329–12337 (2013).
- Luo, J. *et al.* Water photolysis at 12.3% efficiency via perovskite photovoltaics and Earth-abundant catalysts. *Science* **345**, 1593–1596 (2014).
- Smith, R. D. L., Prévot, M. S., Fagan, R. D., Trudel, S. & Berlinguette, C. P. Water oxidation catalysis: electrocatalytic response to metal stoichiometry in amorphous metal oxide films containing iron, cobalt, and nickel. *J. Am. Chem. Soc.* **135**, 11580–11586 (2013).
- Salou, M. *et al.* Initial oxidation of polycrystalline Permalloy surface. *Surf. Sci.* **602**, 2901–2906 (2008).
- Trotochaud, L., Ranney, J. K., Williams, K. N. & Boettcher, S. W. Solution-cast metal oxide thin film electrocatalysts for oxygen evolution. *J. Am. Chem. Soc.* **134**, 17253–17261 (2012).

Acknowledgements

This work was partially supported by the National Science Foundation (grant DMR-1311866), and the Stanford Global Climate and Energy Project. This work was performed in part at the University of Texas Microelectronics Research Center, a member of the National Nanotechnology Coordinated Infrastructure (NNCI), which is supported by the National Science Foundation (grant ECCS-1542159).

Author contributions

L.J. and E.T.Y. contributed to the design concept. L.J., H.-Y.H., X.L., K.H. and Y.Z. performed the fabrication process and measurements. All authors discussed the results and commented on the manuscript.

Additional information

Supplementary information is available in the online version of the paper. Reprints and permissions information is available online at www.nature.com/reprints. Correspondence and requests for materials should be addressed to L.J.

Competing financial interests

The authors declare no competing financial interests.

Methods

Fabrication process. Two types of 4-inch Si (001) wafers were used as substrates in this study. n-Si (phosphorus-doped, $\rho = 0.5\text{--}1\ \Omega\text{cm}$) substrates were used for photoanodes and p-Si (boron-doped, $\rho = 1\text{--}5\ \Omega\text{cm}$) for photocathodes. The Si wafers were first cleaved into $1\text{ cm} \times 1\text{ cm}$ square pieces, followed by cleaning with piranha solution ($\text{H}_2\text{O}:\text{H}_2\text{SO}_4:\text{H}_2\text{O}_2$), buffered oxide etch solution (BOE, $\text{HF}:\text{HCl}:\text{NH}_4\text{F}$) and deionized water (DI), in succession. The back contact was formed by e-beam evaporation of $5\text{nmCr}/100\text{nmAu}$. n-GaAs (100)-oriented (Te-doped, $1 \times 10^{17}\text{ cm}^{-3}$) polished substrates were used for the GaAs-based photoanode. The wafers were cleaned by BOE, acetone, isopropyl alcohol (IPA), deionized water, in succession. The back contact was formed by e-beam evaporation of $10\text{nmNi}/50\text{nmAu}_{88}\text{Ge}_{12}$.

High-quality thermal SiO_2 films were grown at $950\text{ }^\circ\text{C}$ in an oxidation furnace (MRL 8" furnace, Sandvik Thermal Process Inc.) in dry O_2 ambient. This method has been widely used to fabricate gate oxides in MOSFETs with good interfacial quality and low defect density. The p or n-Si/ SiO_2 samples shown in the main manuscript were all grown by this method. For structures in which GaAs was used for the photoanode, high-quality silicon oxides were grown by plasma-enhanced atomic layer deposition (PEALD). In addition, before the deposition of SiO_2 , a 1.5-nm-thick Al_2O_3 layer was first grown by thermal ALD on the GaAs substrate to reduce the interfacial defect density and stabilize the substrate. The silicon oxide PEALD was performed in a Fiji ALD with remote plasma and ozone generator system (Cambridge NanoTech), with tris-dimethylamino-silane and plasma ozone as precursors. The growth temperature was $100\text{ }^\circ\text{C}$ and the growth rate was $\sim 0.8\ \text{\AA}/\text{cycle}$. Remote mode was used, in which the plasma sources were located

remotely from the substrate stage to improve control of the plasma properties. For ALD of TiO_2 and Al_2O_3 we used standard recipes, as described below, in a ALD SavannahTM 200 system (Cambridge NanoTech). The growth temperatures were all set to $200\text{ }^\circ\text{C}$. For TiO_2 , the pulse times for H_2O and tetrakis titanium were 0.015 s and 0.1 s, respectively. For Al_2O_3 , the pulse times for H_2O and trimethylaluminum were 0.015 s and 0.015 s, respectively.

Permalloy (Py) was used as the OER catalyst for all photoanodes and Ti/Pt bilayers were used as HER catalysts for all photocathodes. A series of standard photolithography, e-beam evaporation and lift-off processes were performed to pattern regular array structures on photoelectrodes with various pitch sizes. The thicknesses of Py and Ti/Pt were 150 nm and 30 nm/20 nm, respectively.

Characterization. For electrical test, a tungsten (W) probe tip ($\sim 10\ \mu\text{m}$ radius) and a Lake Shore Cryotronics vacuum probe chamber ($< 1\text{ mtorr}$) were used. $I\text{--}V$ data were collected via an Agilent B1500A device analyser.

Electrochemical measurements were conducted using a CH660D potentiostat (CH Instruments). Before measurement, all the prepared electrolyte was purged by Ar for more than 1 h. A xenon arc lamp was used as light source and was calibrated to 100 mW cm^{-2} . A single-compartment PEC test cell was utilized. A Pt wire and Ag/AgCl/1M KCl electrode (CH Instruments) served as the counter electrode and reference electrode, respectively. Incident-photon-to-photocurrent efficiency was measured using a xenon lamp equipped with a monochromator. The incident light intensity versus wavelength was measured with a standard silicon photodiode. In addition, no sacrificial reagent was used in any of the PEC measurements.